Mineralogical transformations controlling acid mine drainage chemistry

T. Peretyazhko*[1], J. M. Zachara[1], J.-F. Boily[1], Y. Xia[1], P. L. Gassman[1], B. W. Arey[1], W. D. Burgos[2]

[1]Pacific Northwest National Laboratory, Richland, WA 99354

[2] Department of Civil and Environmental Engineering, The Pennsylvania State University, PA, 16802

To be submitted: Chemical Geology

* Corresponding Author: Pacific Northwest National Laboratory, PO Box 999, MS K8-96, Richland, WA 99354; Phone: (509) 376-1529; Fax: (509) 376-3650; E-mail: tetyana.peretyazhko@pnl.gov.

Abstract

The role of Fe(III) minerals in controlling acid mine drainage (AMD) chemistry was studied using samples from two AMD sites [Gum Boot (GB) and Fridays-2 (FR)] located in northern Pennsylvania. Chemical extractions, X-ray diffraction (XRD), scanning electron microscopy (SEM), and Fourier transform infrared spectroscopy (FTIR) were used to identify and characterize Fe(III) phases. The mineralogical analysis revealed schwertmannite and goethite as the principal Fe(III) phases in the sediments. Schwertmannite particles occurred as sub-micron sized spheroids. Their transformation into goethite occurred at the GB site where poorly-crystallized goethite rich in surface-bound sulfate was initially formed. In contrast, no schwertmannite transformation occurred at the FR site. The resulting goethite in GB sediments was also of spherical morphology and resulted from an *in situ* phase transformation involving the conversion of bulk-bound schwertmannite sulfate ions into goethite surface complexes. Chemical extractions moreover showed that the poorly-crystallized goethite particles were subject to further crystallization accompanied by sulfate desorption. Changes in sulfate speciation preceded its desorption, with a conversion of bidentate- to monodentate-bound sulfate surface complexes.

Laboratory sediment incubation experiments were conducted to evaluate the effect of mineral transformation on water chemistry. Incubation experiments were carried out with schwertmannite-containing sediments and aerobic AMD waters with different pH and chemical composition. The pH decreased to 1.9-2.2 in all suspensions and the concentrations of dissolved Fe and S increased significantly. Regardless of differences in the initial water composition, pH, Fe and S were similar in suspensions of the same

sediment. XRD measurements revealed that schwertmannite transformed into goethite in GB and FR sediments during laboratory incubation. The incubation experiments demonstrated that schwertmannite transformation controlled AMD water chemistry under no-flow, batch conditions.

Keywords: acid mine drainage, schwertmannite, mineralogical transformations

1. Introduction

Acid mine drainage (AMD) is produced by biotic and abiotic oxidation of sulfide minerals (ex., pyrite, FeS_2), and the subsequent release of large amounts iron and sulfuric acid (H_2SO_4) to aqueous systems (Bigham et al., 1996; Cravotta, 2008; Malmstrom et al., 2006). Contamination of natural waters with AMD leads to severe acidification and release of toxic elements from mining residues; and induces the erosion, sedimentation and precipitation of Fe(III) minerals (Bigham and Nordstrom, 2000). The extent of damage depends on different controlling factors including the size and buffering capacity of the receiving stream as well as the biogeochemical properties of the AMD (Bigham and Nordstrom, 2000). The physico-chemical, microbiological, and mineralogical processes involved in AMD must therefore be thoroughly understood to evaluate and mitigate their impacts to the environment.

Iron(III) precipitates play a determining role in AMD water quality (Acero et al., 2006; Sullivan and Bush, 2004). For example, the type of Fe(III) mineral formed determines the amount of acidity developed (Dold and Fontbote, 2001). Iron(III) minerals usually found in AMD include jarosite [$KFe_3(SO_4)_2(OH)_6$], goethite [α-FeOOH], ferrihydrite [$Fe_5OH_8{\cdot}4H_2O$] and schwertmannite [$Fe_8O_8(OH)_{8-2x}(SO_4)_x{\cdot}nH_2O$ where $1 \leq x \leq 1.75$] (Bigham et al., 1996; Gagliano et al., 2004; Hochella et al., 1999; Murad and Rojik, 2005; Schwertmann et al., 1995). Jarosite forms at pH<3 and high sulfate concentrations, while ferrihydrite and goethite precipitate at circumneutral pH (Schwertmann and Carlson, 2005). Schwertmannite, on the other hand, is a most common phase precipitating between pH 3 and 4 (Bigham et al., 1996). Schwertmannite acts as an important sink for minor elements (e.g., As, Hg, Pb, Cr) through adsorption or

89 coprecipitation reactions (Bigham and Nordstrom, 2000; Carlson et al., 2002; Espana et
90 al., 2006; Fukushi et al., 2003; Regenspurg and Peiffer, 2005). It can also undergo
91 hydrolysis reactions and consequently be responsible for acidity increase in aqueous
92 environments (Dold and Fontbote, 2001; Sullivan and Bush, 2004).

93 Numerous studies demonstrate that goethite is often present in AMD precipitates
94 dominated by schwertmannite (Bigham et al., 1996; Gagliano et al., 2004; Murad and
95 Rojik, 2005; Schwertmann and Carlson, 2005). Schwertmannite is apparently metastable
96 with respect to goethite, and transforms to this more stable phase by hydrolysis within
97 months to years (Bigham et al., 1996; Gagliano et al., 2004; Murad and Rojik, 2005;
98 Schwertmann and Carlson, 2005) through the reaction:

99 $Fe_8O_8(OH)_{5.5}(SO_4)_{1.25} + 2.5H_2O \rightarrow 8FeOOH + 2.5H^+ + 1.25SO_4^{2-}$ (1)

100 Limited evidence suggests that rate of transformation depends on solution physico-
101 chemical properties, increasing with pH and temperature (Jönsson et al., 2005;
102 Schwertmann and Carlson, 2005), and decreasing with increasing concentrations of
103 sulfate and dissolved organic carbon (Knorr and Blodau, 2007). Recent research has
104 shown that schwertmannite transformation also occurred under anoxic conditions and
105 Fe(II)-catalyzed conversion of schwertmannite to goethite is very rapid (Burton et al.,
106 2008).

107 In this communication we compare the mineralogy of two sites [Gum Boot(GB)
108 and Fridays-2(FR)] that exhibit comparable source AMD discharge compositions, but
109 variable rates of downstream oxygenation, microbiological Fe(II) oxidation, and Fe
110 precipitation rates as described by Senko et al., (2008). A primary goal was to investigate
111 whether relationships existed between the current phase distribution, mineralogic

112 transformation products, and the downstream water composition of the AMD that was
113 different between sites. For this purpose we characterized the morphology, mineralogy,
114 and chemical composition of AMD precipitates with distance from the source terms, and
115 with accumulation depth, using chemical extractions, X-ray diffraction (XRD), and
116 scanning electron microscopy (SEM) with elemental analysis. Additionally, the bulk and
117 surface speciation of sulfate was determined on field-derived AMD precipitates using
118 Fourier- transform infrared spectroscopy (FTIR), with multi-component asynchronous
119 correlation analysis. Laboratory batch incubation experiments were performed with
120 schwertmannite-containing GB and FR sediments and AMD waters of different
121 composition to investigate temporal relationships between water chemistry and AMD
122 mineralogy. We demonstrate that mineralogic transformations of initial AMD
123 precipitates are more closely associated with the evolving surface speciation of sulfate,
124 rather than through the catalytic action of Fe(II).
125
126 **2. Materials and methods**
127 *2.1. Field site and sampling*
128 Two AMD sites were chosen for this study (Senko et al., 2008). The Gum Boot
129 (GB) system is located in McKean County, Pennsylvania (41^{o} 41' 02" N; 78^{o} 29' 37" W),
130 and the Fridays-2 (FR) system is located in Clearfield County, Pennsylvania (41^{o} 14' 34"
131 N; 78^{o} 32' 28" W). At the GB site, AMD emerges at the crest of a hill and flows
132 approximately 18 m downhill in 5 mm sills before flowing underground, reemerging at a
133 point approximately 48 m downhill from the source. Discharge waters enter a pool at the
134 foot of the hill 127 m from the source that subsequently discharge into nearby Gum Boot

Run. Water and surface sediment samples were collected in February and May 2006, at discrete sampling points at 0 m and downstream of the AMD emergence point 2, 9, 15, 60, and 127 m (labeled GB1-GB6). Sediment samples at multiple depths were collected in May 2006 at points 0, 2 and 9 m.

AMD emerges at a former mine entrance at the FR site that flows in sheets (approximately 5 mm deep) approximately 10 m before entering an adjacent unnamed creek. Water and surface sediment samples were collected in February 2006 at discrete sampling points 0 m (the AMD source, FR1), 2, 8 and 10 m downstream from the AMD emergence point. Two additional surface samples were collected at both sites, GB1 and FR1, in July 2006; these samples were used in the incubation experiments (see Section 2.3, "Sediment incubation"). Surface sediments were collected from the top 2 cm of sediment into 50-ml sterile centrifuge tubes. Sediment depth columns were collected using stainless steel split spoons that were driven into AMD sediment.

2.2. Sediment characterization

2.2.1 Extractions and XRD Analyzes

Sediments samples were air-dried and sieved (<2 mm) prior to characterization and incubation.

Ammonium oxalate extraction in the absence of light was performed on each AMD sediment (Bigham et al., 1990; Gagliano et al., 2004; Regenspurg et al., 2004). A 50 mg sediment sample (six replicates) was mixed with ammonium oxalate reagent (28 g/L ammonium oxalate + 15 g/L oxalic acid solution, pH ~2.7). Samples were shaken in the dark for 4 hrs, then centrifuged (3000 rpm, 10 min) and filtered (<0.22 μm). This

158 extraction dissolves poorly-crystalline Fe(III) oxides (ferrihydrite, schwertmannite) in
159 presence of more insoluble crystalline Fe (III) oxides (goethite, hematite) (Cornell and
160 Schwertmann, 2003). Sulfate-rich AMD goethite of poor crystallinity can also be
161 partially dissolved by acid ammonium oxalate (Kumpulainen et al., 2007).

162 The total dissolution of Fe(III) precipitates was performed using 6 M HCl (Gagliano
163 et al., 2004; Regenspurg et al., 2004). A sediment sample of 50 mg (six replicates) was
164 added to 10 mL 6 M HCl. Samples were shaken for 48 hrs, then centrifuged and filtered.

165 Sediment extractions were carried out at pH 10 to evaluate the amount of surface
166 bound sulfate (Kawano and Tomita, 2001). The efficiency of this extraction was
167 evaluated using two sediment samples [GB1 (July) and FR1 (July)] that were dominated
168 by schwertmannite (Fig. S1). Approximately 50-60 % of S_{HCl} (HCl-extractable sulfate)
169 was extracted after 10 min [samples were mixed with pH 10 buffer (NH_4OH/NH_4Cl; 7%
170 NH_4OH, 1% NH_4Cl, 92% H_2O) and immediately centrifuged for 10 min], and up to 80%
171 of S_{HCl} was extracted after 24 hrs (Table S1). X-ray diffraction measurements revealed no
172 change after 10 min of pH 10 extraction. The goethite 110 and 111 peaks, however,
173 became more pronounced after 24 hrs extraction (Fig. S1). Therefore, a 10 min extraction
174 was applied to estimate the amount of adsorbed sulfate in order to avoid any structural
175 changes to AMD mineral phases. For the extraction, 100 mg of sediment (six replicates)
176 was added to 10 mL of pH 10 buffer. The samples were well mixed, immediately
177 centrifuged for 10 min at 3000 rpm, and filtered. The extracted solutions were analyzed
178 for Fe and S by ICP-AES. We assumed that all S extracted from the sediment samples
179 was present in the form of sulfate (hereafter denoted as S), as documented in other studies
180 of AMD sediments (Jönsson et al., 2005).

Powder X-ray diffraction patterns of the sediments were recorded using a high-resolution Ω-2Θ Four-Circle X-ray Diffractometer (Philips X'Pert MRD PRO, Philips Co., Sunnyvale, CA). Intensities were measured with a 0.02° step size and 2 s counting time per step.

2.2.2. SEM

Whole mount samples were prepared for SEM imaging by fixation to carbon tape. Air-dried sediments were also fixed with EpoThin epoxy (Buehler) to prepare thin sections. Samples were dried overnight, cemented to quartz optical grade microscope slides (25.4 mm x 25.4 mm x 1 mm, SPI), sectioned [Isomet 1000 diamond blade thin sectioning saw (Buehler) with Isocut fluid] and polished [aluminum oxide sand paper, TEXMET 1000 (Buehler) and 1 micron diamond polish (Metadi II , Buehler)]. Imaging and EDS analysis were performed using a LEO82 field emission SEM operating at 3 kV fitted with backscattered and secondary electron detectors, coupled with an Oxford EDS system.

2.2.3 FTIR

The FTIR of the GB samples were collected as a function of distance from the AMD source (GB1, GB3, GB5) and as a function of depth (GB1D depth samples) using the KBr technique. The measurements were carried out on a Bruker IFS 66v/S FTIR spectrometer, equipped with a Globar source, KBr beam splitter, MCT detector and OPUS operating software. Each spectrum was derived from 512 co-added scans collected in transmission mode in the 2000–800 cm^{-1} range with a spectral resolution of 4 cm^{-1}. All spectra were expanded to a Two-Dimensional Asynchronous correlation map (Noda and Ozaki, 2004) using the code of Boily and Ilton (2008). This map allowed identification of

204 the precise positions of the various S-O stretching vibration bands of sulfate associated
205 with various Fe(III) minerals. All calculations and mapping procedures were performed
206 with Matlab (The Mathworks, Inc.).
207 The spectra were used to document changes in (1) the bulk and surface speciation of
208 sulfate (S-O stretching vibrations) and (2) the mineralogical compositions as a function of
209 distance and depth from the AMD source. Our interpretations are supported by the
210 results of an unpublished study in which we followed the effects of pH and dehydration
211 on the speciation of bulk and surface-bound sulfate ions in synthetic schwertmannite. Our
212 study shows that dehydration does not considerably affected band positions, although it
213 does promote the formation of a minor bisulfate component. The pH dependence of the
214 spectra of schwertmannite were in fact highly comparable to *in situ* measurements of
215 Jönsson et al. (2005) with three dominant forms of sulfate that will be further discussed in
216 Section 3.2.3.
217
218 *2.3. Sediment incubation*
219 Incubation experiments (310 d) were performed to investigate transformations of
220 metastable mineral phases in the sediment, and associated changes in AMD water
221 chemistry. The <2 mm size fraction of the air-dried GB1 (July) and FR1 (July) samples
222 were used in two series of sediment incubations, one with GB4 water and another with
223 GB6 water. The sediments contained mainly schwertmannite with traces of goethite by
224 XRD (Fig. S1, Table 1), and displayed similar Fe and S contents (Table 1). The N_2-BET
225 specific surface areas were 190 m^2/g (GB1) and 180 m^2/g (FR1), with pore sizes of less

than 20 Å. The two waters used for incubation had different compositions (Table S2); GB4 was more acidic, and contained higher concentrations of Fe, S and other elements.

Sediment suspensions were prepared by mixing 10 g of the sediments with 200 mL of AMD water in 250-mL plastic bottles. Two replicates were prepared for each treatment [GB1 sediment + GB4 water (GB1s_GB4w), GB1 sediment + GB6 water (GB1s_GB6w), FR1 sediment + GB4 water (FR1s_GB4w), and FR1 sediment + GB6 water (FR1s_GB6w)]. pH was measured at selected time points, and suspension subsamples were collected and centrifuged (3000 rpm, 10 min) for phase separation. The resulting aqueous phase was analyzed for Fe and S by ICP-AES. The sediment samples were air-dried, and then extracted with ammonium oxalate and pH 10 buffer.

2.4. Thermodynamic calculations

Saturation indices were calculated for schwertmannite and goethite using PHREEQC [Version 2.14, (Parkhurst and Appelo, 1999)]. The solubility product constants (K_{sp}) were taken from Bigham et al (1996) for the two following reactions:

$Fe_8O_8(OH)_x(SO_4)_y + (24\text{-}2y)H^+ = 8Fe^{3+} + ySO_4^{2-} + (24\text{-}2y+x)/2H_2O$;

$$\log K_{sp} = 18.0 \pm 2.5 \qquad (2)$$

$FeOOH + 3H^+ = Fe^{3+} + 2H_2O$; $\log K_{sp} = 1.4 \pm 0.01$ (3)

From Eqns. 2 and 3 and the solubility products, the following stability relationships were obtained

schwertmannite: $pa_{Fe3+} = -2.82 + 2.6pH$ (4)

and goethite: $pa_{Fe3+} = -1.4 + 3pH$ (5)

where $pa_{Fe3+} = -\log a_{Fe3+}$, a_{Fe3+} = the activity of Fe^{3+}. Eqn. (4) was fixed with an average $pa_{SO42-} = 2.84 \pm 0.16$ [calculated based on dissolved S, Fe and pH (Fig. 8) using PHREEQC], $x = 4.8$ and $y = 1.6$ [Eqn. (2), Bigham et al, 1996]. Variation in pa_{SO42-} didn't result in significant changes in the calculated paFe3+, therefore, the solubility line of schwertmannite was calculated only with the average $pa_{SO42-} = 2.84$.

3. Results and discussion

3.1. AMD water chemistry

Seasonal variations in pH and dissolved concentrations of Fe(II) and S were not significant at GB and FR sites. Representative distributions of aquatic physico-chemical parameters measured in February are shown in Fig. 1. The aqueous phase of the GB AMD contains ~0.9 mM Fe(II) at the emergence point (GB1). Iron(II) was however completely removed from GB AMD waters after 15 m of downstream movement (Fig. 1b). Iron(II) removal from FR waters was less extensive due to different hydrological conditions [flow rate (50 and 136 L/min at GB and FR, respectively (Senko et al., 2008); distance from source to stream junction (127 and 10 m at GB and FR, respectively)]. Dissolved Fe(II) was detected at all FR sampling points with an average concentration of 2.2±0.2 mM (Fig. 1d). Average concentrations of dissolved S were higher at FR (4.04±0.13 mM) than at GB (1.19±0.04 mM) (Fig. 1b,d). Dissolved S concentration did not change significantly with distance from the source at both sites (Fig. 1b,d). The pH varied between 4.5-4.1 (source) to 3.7-3.9 downhill at both AMD sites (Fig. 1a,c). Low pH and high concentrations of dissolved S could be attributed not only to oxidation of

sulfide minerals (Bigham et al., 1996; Cravotta, 2008; Malmstrom et al., 2006) but to post deposition mineralogical transformations in the AMD sediments.

3.2. AMD mineralogy

3.2.1. XRD

XRD analyses of the GB1-4 sediments collected in February downhill from the source to the point where water flows underground revealed that goethite was the dominant mineral. Goethite and quartz were present in GB 5-6 samples, i.e. downhill of water reemergence (Table 1). The mineralogy of the GB samples collected in May and July was significantly different for sites located in the source proximity (0-2 m). The summer samples of both GB1 and GB2 were composed primarily of schwertmannite, with some goethite in GB1 (Fig. 2a,b). No mineralogical changes were observed downhill of this location, and goethite remained the principal phase (ex. GB3, Fig. 2c). The presence of goethite together with schwertmannite, or goethite alone confirmed that schwertmannite was metastable with respect to goethite in these systems (Bigham et al., 1996; Gagliano et al., 2004; Murad and Rojik, 2005; Schwertmann and Carlson, 2005). Such changes in the initial precipitate mineralogy of the GB surface sediment might be due to seasonal variations in aqueous composition, water flow rate, and/or temperature. For instance, Kumpulainen et al (2007) observed that schwertmannite formed in spring after snowmelt, but was partially transformed into goethite during warmer summer months. Drying led to precipitate cementation that limited S and H^+ diffusion, and prevented full conversion of schwertmannite to goethite (Kumpulainen et al., 2007).

Cementation of the upper layers of mineral precipitates was common at both GB and FR sites.

The results of XRD analysis of the GB sediment depth series revealed no mineralogical changes at the GB3D site, where goethite was the principal mineral (Table 1). X-ray diffraction analysis of the GB1D depth series showed that the upper 0.3 m was composed primarily of schwertmannite with a trace amount of goethite (Fig. 3, Table 1). The dominant phase in the two deepest samples of the GB1D column (0.6-1.1 m) was goethite (Fig. 3). The middle portion of the GB1D column (0.35-0.55 m) represented a transition zone where the proportion of schwertmannite decreased, as goethite increased with depth. Similar transitions of schwertmannite to goethite with sediment depth were observed for the GB2 site. To summarize, the XRD study of the GB sediments demonstrated that mineralogical transformations occurred at both the surface and with depth in the AMD sediments.

The dominant mineral phase of samples FR1 through FR4 (February) was schwertmannite (Table 1). Along with schwertmannite, X-ray patterns of the FR4 displayed weak reflections of goethite (Table 1). The XRD data for the FR1 (July) sample showed that schwertmannite was the principal Fe(III) phase. It, however, also contained the traces of goethite. Comparison of the XRD data of the two FR samples collected at different times (February and July) showed that schwertmannite was the dominant phase, possibly due to slow mineralogical changes.

3.2.2. SEM

SEM analysis of GB1D (0-0.15 m, May) revealed that schwermannite formed spherical particles of 1-2 μm diameter (Fig. 4a,b) that were associated in larger aggregates. The spherical particles of FR1 (February) schwertmannite had glassy, molten-like surfaces (Fig. 4c,d). Characteristic filamentous features (Cornell and Schwertmann, 2003) were not evident for any of the schwertmannite spherical particles in GB1D (0-0.15 m, May) and FR1 (February). The "pin-cushion" or filamentous morphology has been observed in loose precipitates but might be absent for schwertmannite from cemented GB and FR sediments (Bigham and Nordstrom, 2000).

SEM analysis also showed that GB1 (February) goethite particles exist as spheres (Fig. 4e,f) with morphology common to schwertmannite. Some of the goethite particles were hollow inside, while schwertmannite particles were firm and filled (Fig. 4 a,b,e,f, Fig. 5). The hollow goethite particles may form through dissolution of schwertmannite inside the spheres (Yu et al., 2003); however, further investigation is required. The spherical goethite morphology may be relict (pseudomorphic) from schwertmannite that was preserved during recrystallization. Others have noted that goethite can adopt the initial schwertmannite morphology and size (Jönsson et al., 2005; Schwertmann and Carlson, 2005; Sullivan and Bush, 2004). This relationship suggests a 1:1 transformation of schwertmannite aggregates into those of goethite (Schwertmann and Carlson, 2005).

Whole mount thin sectioned SEM analysis showed that the average Fe/S ratios of GB1D (0-0.15 m, May), FR1 (February) and GB1 (February) were 8 ± 3, 9 ± 2 and 21 ± 5, respectively (Fig. 5). The Fe/S ratios for the GB1D (0-0.15 m, May) and FR1 (February) samples were within the range of that reported for schwertmannite (5.3-8, Bigham et al 1990).

337

338 *3.2.3. FTIR*

339 All GB samples exhibited the characteristic in-plane (δ_{OH}) and out-of-plane (γ_{OH})
340 deformation modes of goethite at ~900 and ~800 cm^{-1} (Fig. 6), respectively, consistent
341 with the XRD analyses showing the importance of this phase. The O-H stretching region
342 (not shown) also displayed the important ~3100 cm^{-1} band of goethite. The O-H
343 stretching region in the GB1D samples (0-0.55 m) revealed a secondary feature centered
344 at ~3400 cm^{-1} arising from schwertmannite, an observation consistent with the XRD
345 analyses (Fig. 3). The infrared data are, as a whole, consistent with the XRD analyses and
346 confirm the presence of both goethite and schwertmannite in the sediments.

347 The spectra of the sediment samples collected as a function of depth (GB1D
348 sediments) and distance from the AMD source (GB1, GB3, GB5) were used to generate
349 an asynchronous 2D correlation map to identify the important sulfate vibrational modes.
350 The resulting map (Fig. 7c) reveals peaks at 1215, 1135, 1088, 1065, 1010 and 985
351 cm^{-1} resulting for symmetric and asymmetric S-O stretching vibrations of sulfate
352 molecules. These modes, which are identified for sediment sample GB1D (0.35-0.55 m)
353 (Fig. 7b) are comparable to those of the pure component spectra for three predominant
354 mineral-bound sulfate geometries (Fig. 7a) that were resolved in another study from our
355 group (unpublished). The 1215, 1135 and 985 cm^{-1} bands correspond to the C_{2v} geometry
356 of sulfate [that is, a sulfate bidentate complex (Peak et al., 1999) in the schwertmannite
357 structure and/or at the Fe(III) oxide surface, and/or strongly hydrogen-bonded complexes
358 (Majzlan and Myneni, 2005)]. The 1135, 1065 and 985 cm^{-1} bands arise, on the other
359 hand, from sulfate surface complexes of C_{3v} symmetry [a monodentate sulfate complex

360 (Peak et al., 1999) at the Fe(III) oxide surface]. The presence of the both sets of bands
361 therefore denote the existence of both types of surface complexes in the AMD Fe(III)
362 precipitates. A third complex that is hydrogen-bonded or physisorbed (T_d, Peak et al.
363 1999; Jönsson et al. 2005) is also present.

364 The GB1 sediment exhibits the strongest degree of ν_3 splitting and therefore the
365 strongest proportion of bidentate sulfate complexes of C_{2V} symmetry (Fig. 6a). A
366 decrease in ν_3 splitting occurs with distance from the AMD source, implying conversion
367 of bidentate C_{2V} complexes to monodentate C_{3V}-type complexes on the goethite surface.
368 Similar to GB surface samples (Fig. 6a), the speciation of sulfate as a function of
369 sediment depth also exhibits a decrease in the intensity of the high-energy ν_3 band,
370 denoting a change from the C_{2V} symmetry of the schwertmannite-bound sulfate complex
371 at the surface of GB1D to a C_{3V} symmetry for sulfate bound to the surface of goethite
372 particles present in the deeper sediments (Fig. 6b). Going from the surface [GB1D (0-
373 0.15 m)] to deeper sediments [GB1D (0.35-0.55 m) and GB1D (0.9-1.1 m], also increases
374 the relative importance of goethite bands (e.g. the in-plane and out-of-plane) relative to
375 the area of the S-O stretching area, a result that is consistent with the EDS spectra of Fig.
376 5 in terms of the Fe/S ratios and XRD results (Fig. 3).

377

378 *3.3. Chemical extractions of the AMD sediments*

379 The amount of oxalate extracted Fe from the GB (February) surface samples
380 decreased from 94 % to 2 % of Fe_{HCl} downhill from the emergence point due to an
381 increase in goethite crystallinity (Table 1). The concentration of Fe_{HCl} decreased along the
382 profile as well, through dilution of the Fe(III) phases with quartz (Table 1). Similarly, the

383 S content decreased with distance from the source (Table 1). Up to 51-97% of S_{HCl} was
384 extracted at pH 10 from the GB samples indicating that most of the S was associated with
385 the goethite surface. Overall, the poorly-crystalline, S-rich goethite was located near the
386 GB source; its crystallinity increased downstream while S content decreased.

387 The concentrations of S_{ox} and S_{HCl} in the schwertmannite-containing GB surface
388 samples [GB1D(0-0.15 m, May), GB2D(0-0.15m, May) and GB1 (July)] were close to
389 or slightly higher than those of the goethite-containing GB1 (February) and GB2
390 (February) samples, respectively, while S_{pH10} was 0.23-0.28 mmol/g lower (Table 1).
391 These results implied that there was little release of structural S during the
392 schwertmannite transformation, and that most of the S became surface-complexed.
393 Concentrations of extractable S from GB schwertmannite and goethite were in good
394 agreement with the laboratory study of Schwertmamm and Carlson (2005), where the
395 conversion of schwertmannite was shown to result in the adsorption of considerable
396 amounts of sulfate to the goethite surface. These authors hypothesized that sulfate
397 adsorption caused the spherical morphology of goethite.

398 In contrast to GB, the concentration of the oxalate-extractable Fe in the FR
399 samples averaged ~6.7 mmol/g and did not change significantly with distance from the
400 source or sampling time [FR1 (February and July)]. The Fe_{ox}/Fe_{HCl} ratio ranged from
401 85% to 94% because schwertmannite was the principal Fe(III) phase (Table 1). The
402 average chemical formula of schwertmannite obtained from the oxalate extraction data
403 was $Fe_8O_8(OH)_{5.56}(SO_4)_{1.22}$.

404 Vertical profiles at the GB1 (May) and GB2 (May) sites showed similar Fe and S
405 depth trends (Table 1). The oxalate extracted Fe decreased with depth, while Fe_{HCl}

406 slightly increased, indicating an increase in goethite crystallinity. Similar to the GB
407 (February) surface samples, the increase in crystallinity was accompanied by a drop in S
408 content. The vertical distribution therefore showed that mineralogical changes from
409 schwertmannite to goethite at GB1 (May) and GB2 (May) sites were accompanied by an
410 increase in goethite crystallinity concomitant with the depletion of sulfate. In the
411 sediment depth samples, 67-100% of S_{HCl} was extracted at pH 10, indicating that the
412 majority of S was surface bound to goethite and schwertmannite. The average chemical
413 formula of schwertmannite obtained from the oxalate extraction data of GB1 and GB2
414 depth samples was similar to the one found for the FR schwertmannite.

415 To summarize, the results of mineralogical analysis showed that schwertmannite
416 transformation occurred at GB site. Little release of sulfate occurred into aqueous
417 solution during the transformations and the initially formed goethite was poorly-
418 crystallized and rich in surface bound sulfate. The goethite had spherical morphology due
419 to preservation of schwertmannite structure by adsorbed sulfate. The poorly-crystallized
420 goethite was subject to further crystallization accompanied by S desorption to the
421 aqueous phase. Changes in surface speciation preceded sulfate desorption, with a
422 conversion from C_{2v} to C_{3v} symmetry. Further experimental study is however necessary
423 to evaluate the effect of the mineral transformation on water chemistry.

424 *3.4. Sediment incubation*

425 Incubation experiments were performed to study the influence of schwertmannite
426 transformation on AMD waters that differ in pH and composition (GB4w and GB6w,
427 Table S2). The pH values in all suspensions gradually decreased during incubation to
428 ~2.2 (GB1 sediments) and ~1.9 (FR1 sediments) (Fig. 8). Unlike the suspensions with

GB4 water, for which no shift in the initial pH value was observed, mixing GB1 and FR1 sediments with GB6 water (initial pH = 5.15, Table S2) resulted in an immediate pH drop from 5.15 to 2.9. When the aqueous phase was replaced in the GB1s_GB6w and FR1_GB6w suspensions after approximately 100 d, the pH value still dropped to 2.9 within one day (Fig. 8, note arrows). The pH decrease was due to schwertmannite acidity which made it a significant proton source (Bigham et al., 1996; Gagliano et al., 2004; Murad and Rojik, 2005; Schwertmann and Carlson, 2005). Based on the average schwertmannite composition of $Fe_8O_8(OH)_{5.56}(SO_4)_{1.22}$ determined by oxalate extraction (Table 1), around 0.3 mol H^+ could be released per mole of Fe^{3+} upon hydrolysis to goethite, a result that is in agreement with published data [0.26-0.40 mol H^+;(Bigham et al., 1996; Kawano and Tomita, 2001; Peine et al., 2000)]. The decrease in pH was accompanied by an increase in dissolved Fe and S (Fig. 8).

At the end of incubation, the Fe and S concentrations were lower in GB1 suspensions [11.61±0.12 mM and 10.76±0.78 mM S; 4.40±0.06 mM and 3.85±0.49 mM Fe in the GB1s_GB4w and GB1s_GB6w, respectively] than in the FR1 suspensions [37.61±1.05 mM and 40.51±0.29 mM S; 16.43±0.87 mM and 15.98±0.08 mM Fe in FR1s_GB4w and FR1s_GB6w, respectively]. Regardless of differences in the initial composition of GB4w and GB6w (Table S2), the final concentrations of Fe and S were of comparable order of magnitude in suspensions of the same sediment (e.g., GB1s_GB4w and GB1s_GB6w). Calculation of saturation indices revealed that all sediment suspensions were undersaturated with respect to schwertmannite and supersaturated with respect to goethite (Fig. 9). Thus, dissolution and/or transformation of schwertmannite controlled the chemical composition of the aqueous phase (i.e., pH and S content).

452 Mineralogical changes were significant in the GB1 and FR1 incubations, where
453 XRD analysis revealed that goethite was the principal Fe(III) mineral at experiment
454 termination (Fig. S3). The concentration of Fe_{ox} began to decrease after approximately
455 128 d coincident with goethite crystallization (Fig. S4). We unexpectedly found that the
456 schwertmannite to goethite transformation occurred under laboratory conditions in FR1.
457 This observation contrasted with the XRD analysis of the FR sediments (May and
458 February) that revealed no significant goethite formation in FR sediments (Table 1). This
459 difference might be explained by different field and laboratory temperature and chemical
460 conditions, and the influence of AMD advection over and within the Fe(III) deposits. It is
461 possible that the rate of schwertmannite precipitation and accretion was faster than its
462 transformation into goethite at the FR site. Further laboratory and field studies are
463 required to resolve this interesting disparity.
464 The laboratory incubation experiments demonstrated that schwertmannite
465 dissolution and/or transformation controlled AMD water chemistry under no-flow, batch
466 conditions. AMD properties (acidity, dissolved S) are therefore regulated by two
467 important sources: (i) primary sulfide minerals (pyrite, pyrrhotite) and (ii) secondary
468 metastable Fe(III) phases formed after Fe^{2+} oxidation.
469
470 *3.5. Environmental implications*
471 Our results demonstrate an important relationship between mineralogical
472 transformations and the water composition of AMD. Conversion of schwertmannite to
473 goethite leads to decrease in pH and increase in the dissolved concentration of sulfate
474 (Fig. 10) as found in laboratory incubations of AMD sediments [this work; (Bigham et

al., 1996; Jönsson et al., 2005; Knorr and Blodau, 2007; Schwertmann et al., 1995)] and in field conditions (Kumpulainen et al., 2007). At GB and FR sites, the noted pH decrease from 4.1-4.5 (source) to 3.7-3.9 downhill (Fig. 1a,c) could, therefore, be explained by Fe(II) oxidation to Fe(III) with subsequent precipitation (Senko et al., 2008) and by conversion of secondary metastable Fe(III) phases (e.g., schwertmannite). However, the dissolved S concentration in GB and FR systems does not change significantly between sampling points (GB1-6, FR1-4) or sampling time (February and May) (Fig. 1 b,d). Average concentrations of dissolved S were higher at FR (4.04±0.13 mM) than at GB (1.19±0.04 mM). Such uniform S concentrations over time and with distance from the source may be explained by a low (as compared to flow) rate of S release from Fe(III) solid phases and/or by reprecipitation of the released S in schwertmannite (Fig. 10).

Other field measurements [such as, schwertmannite precipitation/accretion rate and its transformation into goethite, rate of sulfate release from sediments, pore water composition] are needed to fully interpret factors controlling AMD water and sediment composition.

Acknowledgements

We thank John Senko and Melanie Lucas (Pennsylvania State University) for providing us with sediment and water samples. We are grateful to Tom Resch (PNNL) for thin sections preparation. We thank Ravi Kukkadapu (PNNL) for valuable discussions on the interpretation of AMD mineralogy data. XRD, SEM and FTIR analysis were performed

498 in the Environmental Molecular Sciences Laboratory (EMSL) that is managed and
499 supported by OBER-ERSD. PNNL is operated for the DOE by Battelle. This work was
500 partially supported by the National Science Foundation under Grant No. CHE-0431328
501 and the U.S. Department of Energy, Biological and Environmental Research (BER).
502

References

Acero, P., Ayora, C., Torrento, C. and Nieto, J.M., 2006. The behavior of trace elements during schwertmannite precipitation and subsequent transformation into goethite and jarosite. Geochimica et Cosmochimica Acta, 70(16): 4130-4139.

Bigham, J.M. and Nordstrom, D.K., 2000. Iron and aluminum hydroxysulfates from acid sulfate waters. In: C.N. Alpers, J.L. Jambor and D.K. Nordstrom (Editors), Sulfate minerals, crystallography, geochemistry and environmental significance. Reviews in mineralogy and geochemistry, Mineralogical Society of America, Washington, D.C., pp. 351-403.

Bigham, J.M., Schwertmann, U., Carlson, L. and Murad, E., 1990. A poorly crystallized oxyhydroxysulfate of iron formed by bacterial oxidation of Fe(II) in acid-mine waters. Geochimica et Cosmochimica Acta, 54(10): 2743-2758.

Bigham, J.M., Schwertmann, U., Traina, S.J., Winland, R.L. and Wolf, M., 1996. Schwertmannite and the chemical modeling of iron in acid sulfate waters. Geochimica et Cosmochimica Acta, 60(12): 2111-2121.

Boily, J.-F., Ilton, E.S., 2008. An independent confirmation of the correlation of Uf4 primar peaks and satellite structures of U^{VI}, U^{V} and U^{IV} in mixed valence uranium oxides by two-dimensional correlation spectroscopy. Surface Sci. 602, 3637-3646.

Carlson, L., Bigham, J.M., Schwertmann, U., Kyek, A. and Wagner, F., 2002. Scavenging of As from acid mine drainage by schwertmannite and ferrihydrite: a comparison with synthetic analogues. Environmental Science and Technology, 36(8): 1712-1719.

526 Cornell, R.M. and Schwertmann, U., 2003. The iron oxides: structure, properties,
527 reactions, occurrences and uses. Wiley-VCH, New York, 664 pp.
528 Cravotta, C.A., 2008. Dissolved metals and associated constituents in abandoned coal-
529 mine discharges, Pennsylvania, USA. Part 2: geochemical controls on constituent
530 concentrations. Applied Geochemistry, 23(2): 203-226.
531 Dold, B. and Fontbote, L., 2001. Element cycling and secondary mineralogy in porphyry
532 copper tailings as a function of climate, primary mineralogy, and mineral
533 processing. Journal of Geochemical Exploration, 74(1-3): 3-55.
534 Espana, J.S., Pamo, E.L., Pastor, E.S., Andres, J.R. and Rubi, J.A.M., 2006. The removal
535 of dissolved metals by hydroxysulphate precipitates during oxidation and
536 neutralization of acid mine waters, Iberian Pyrite Belt. Aquatic Geochemistry,
537 12(3): 269-298.
538 Fukushi, K. et al., 2003. A natural attenuation of arsenic in drainage from an abandoned
539 arsenic mine dump. Applied Geochemistry, 18(8): 1267-1278.
540 Gagliano, W.B., Brill, M.R., Bigham, J.M., Jones, F.S. and Traina, S.J., 2004. Chemistry
541 and mineralogy of ochreous sediments in a constructed mine drainage wetland.
542 Geochimica et Cosmochimica Acta, 68(9): 2119-2128.
543 Hochella, M.F., Moore, J.N., Golla, U. and Putnis, A., 1999. A TEM study of samples
544 from acid mine drainage systems: metal-mineral association with implications for
545 transport. Geochimica et Cosmochimica Acta, 63(19-20): 3395-3406.
546 Jönsson, J., Persson, P., Sjoberg, S. and Lovgren, L., 2005. Schwertmannite precipitated
547 from acid mine drainage: phase transformation, sulphate release and surface
548 properties. Applied Geochemistry, 20(1): 179-191.

549 Kawano, M. and Tomita, K., 2001. Geochemical modeling of bacterially induced
550 mineralization of schwertmannite and jarosite in sulfuric acid spring water.
551 American Mineralogist, 86(10): 1156-1165.
552 Knorr, K.H. and Blodau, C., 2007. Controls on schwertmannite transformation rates and
553 products. Applied Geochemistry, 22(9): 2006-2015.
554 Kumpulainen, S., Carlson, L. and Raisanen, M.L., 2007. Seasonal variations of ochreous
555 precipitates in mine effluents in Finland. Applied Geochemistry, 22(4): 760-777.
556 Majzlan, J. and Myneni, S.C.B., 2005. Speciation of iron and sulfate in acid waters:
557 aqueous clusters to mineral precipitates. Environmental Science and Technology,
558 39(1): 188-194.
559 Malmstrom, M.E., Gleisner, M. and Herbert, R.B., 2006. Element discharge from pyritic
560 mine tailings at limited oxygen availability in column experiments. Applied
561 Geochemistry, 21(1): 184-202.
562 Murad, E. and Rojik, P., 2005. Iron mineralogy of mine-drainage precipitates as
563 environmental indicators: review of current concepts and a case study from the
564 Sokolov Basin, Czech Republic. Clay Minerals, 40(4): 427-440.
565 Noda, I. and Ozaki, Y., 2004. Two-dimensional correlation spectroscopy-applications in
566 vibrational and optical spectroscopy. John Wiley and Sons, New York.
567 Parkhurst, D.L. and Appelo, C.A.J., 1999. User's guide to PHREEQC (version 2)- a
568 computer program for speciation, batch-reaction, one-dimentional transport, and
569 inverse modeling. U.S. Geological Survey Water-Resources Investigations Report
570 99-4259.

571 Peak, D., Ford, R.G. and Sparks, D.L., 1999. An in situ ATR-FTIR investigation of
572 sulfate bonding mechanisms on goethite. Journal of Colloid and Interface Science,
573 218(1): 289-299.
574 Peine, A., Tritschler, A., Kusel, K. and Peiffer, S., 2000. Electron flow in an iron-rich
575 acidic sediment - evidence for an acidity-driven iron cycle. Limnology and
576 Oceanography, 45(5): 1077-1087.
577 Regenspurg, S., Brand, A. and Peiffer, S., 2004. Formation and stability of
578 schwertmannite in acidic mining lakes. Geochimica et Cosmochimica Acta,
579 68(6): 1185-1197.
580 Regenspurg, S. and Peiffer, S., 2005. Arsenate and chromate incorporation in
581 schwertmannite. Applied Geochemistry, 20(6): 1226-1239.
582 Schwertmann, U., Bigham, J.M. and Murad, E., 1995. The first occurrence of
583 schwertmannite in a natural stream environment. European Journal of
584 Mineralogy, 7(3): 547-552.
585 Schwertmann, U. and Carlson, L., 2005. The pH-dependent transformation of
586 schwertmannite to goethite at 25ºC. Clay Minerals, 40(1): 63-66.
587 Senko, J.M., Bruns, M.A. and Burgos, W.D., 2008. Characterization of Fe(II) oxidizing
588 bacterial activities and communities at two acidic Appalachian coal mine
589 drainage-impacted sites. submitted to The ISME Journal: Multidisciplinary
590 Journal of Microbial Ecology.
591 Sullivan, L.A. and Bush, R.T., 2004. Iron precipitate accumulations associated with
592 waterways in drained coastal acid sulfate landscapes of eastern Australia. Marine
593 and Freshwater Research, 55(7): 727-736.

Yu, S.H., Colfen, H. and Antonietti, M., 2003. Polymer-controlled morphosynthesis and mineralization of metal carbonate superstructures. Journal of Physical Chemistry B, 107(30): 7396-7405.

Figure captions

Fig. 1. Distributions of aquatic physico-chemical parameters as a function of distance from source: (a) and (b) GB; (c) and (d) FR.

Fig. 2. X-ray powder diffraction patterns of the GB sediment samples collected in February and May: (a) GB1; (b) GB2; (c) GB3. gt-goethite, sh-schwertmannite.

Fig. 3. X-ray powder diffraction patterns of the GB1D sediment samples collected at different depths.

Fig. 4. Scanning electron microscopy images of (a) and (b) GB1D (0-0.15 m) collected in May; (c) FR1, (d) FR4, (e) and (f) GB1 collected in February.

Fig. 5. Scanning electron microscopy images of thin sections and corresponding EDS spectra of (a) GB1D (0-0.15 m) collected in May; (b) FR1 and (c) GB1 collected in February.

Fig. 6. FTIR spectra of (a) GB surface samples collected in February and (b) GB1D sediment samples collected at different depths in May.

Fig. 7. FTIR spectra of (a) pure sulfate components resolved for synthetic schwertmannite (unpublished), (b) GB1D (0.35-0.55 m) and (c) asynchronous 2D correlation map built from FTIR spectra shown in Fig. 6.

Fig. 8. Dissolved Fe, S and pH as a function of incubation time. Sediment suspensions are (a) GB1s_GB4w; (b) GB1s_GB6w; (c) FR1s_GB4w; (d) FR1s_GB6w. Error bars show standard deviation (two replicates). Arrows denote time when aqueous phase was replaced.

Fig. 9. Plots of $pa_{Fe^{3+}}$ vs pH for the sediment suspensions. The solubility lines of schwertmannite and goethite were calculated by Eqns. (4) and (5) for pa_{SO42-} =

622 2.84. Dotted lines are boundaries of the solubility window of schwertmannite.
623 Solubility products of schwertmannite and goethite were taken from Bigham et al
624 1995.
625 Fig. 10. Schematic of schwertmannite conversion to well-crystallized goethite based on
626 results of mineralogical analysis and laboratory incubation of AMD sediments.
627
628
629
630
631

Table 1 Mineralogy of the GB and FR precipitates and concentrations of oxalate, 6 M HCl and pH 10 extracted Fe and S.

Sample	Location, m	XRD	Fe_{ox}	Fe_{HCl}	S_{ox}	S_{HCl}	S_{pH10}
					mmol/g		
surface sediments (collected in February 2006)							
GB1	0	gt	6.41±0.21	8.56±0.09	1.00±0.02	1.12±0.02	0.97±0.02
GB2	2	gt	7.91±0.28	8.43±0.29	1.26±0.02	1.30±0.04	1.04±0.02
GB3	9	gt	5.62±0.33	9.13±0.27	0.65±0.02	0.74±0.02	0.57±0.01
GB4	15	gt	5.23±0.14	9.05±0.08	0.62±0.01	0.74±0.01	0.55±0.01
GB5	60	gt, qz	0.17±0.04	7.81±0.19	0.26±0.02	0.51±0.01	0.32±0.02
GB6	127	gt, qz	0.18±0.03	4.09±0.08	0.08±0.01	0.14±0.01	0.08±0.01
FR1	0	sh	7.28±0.13	8.23±0.09	1.30±0.00	1.36±0.00	1.20 ±0.01
FR2	2	sh	6.51±0.06	7.65±0.17	1.19±0.00	1.37±0.03	0.92±0.02
FR3	8	sh	6.76±0.72	7.93±0.21	1.27±0.05	1.43±0.01	0.85±0.01
FR4	10	sh, gt	6.94±0.55	7.36±0.15	1.20±0.02	1.37±0.03	1.22±0.03
surface sediments (collected in July 2006)*							
GB1	0	sh, gt	6.81±0.34	7.20±0.29	1.32±0.09	1.42±0.06	0.69±0.02
FR1	0	sh, gt	6.68±0.16	6.89±0.14	1.40±0.13	1.40±0.11	0.83±0.04
vertical profiles (collected in May 2006)							
GB1D	0-0.15	sh, gt	5.05±0.13	8.15±0.18	0.95±0.02	1.03±0.00	0.74±0.01
GB1D	0.15-0.3	sh, gt	7.22±0.11	8.34±0.12	0.95±0.00	1.07±0.00	0.68±0.01
GB1D	0.35-0.55	gt, sh	6.24±0.20	8.56±0.25	0.72±0.01	0.81±0.01	0.61±0.02
GB1D	0.6-0.8	gt	5.17±0.23	9.07±0.14	0.52±0.01	0.63±0.00	0.57±0.01
GB1D	0.9-1.1	gt	3.49±0.13	9.53±0.22	0.31±0.01	0.42±0.01	0.35±0.01
GB2D	0-0.15	sh	7.26±0.41	7.76±0.22	1.18±0.03	1.32±0.00	0.79±0.02
GB2D	0.15-0.5	sh, gt	7.69±0.37	7.99±0.05	1.12±0.01	1.19±0.01	0.77±0.01
GB2D	0.6-0.8	gt	2.52±0.07	9.01±0.12	0.36±0.00	0.46±0.03	0.37±0.01
GB3D	0-0.15	gt	2.27±0.06	9.66±0.14	0.40±0.01	0.54±0.02	0.41±0.01
GB3D	0.2-0.4	gt	2.72±0.14	9.27±0.21	0.42±0.00	0.51±0.00	0.40±0.14
GB3D	0.4-0.6	gt	2.80±0.11	8.32±0.22	0.37±0.01	0.45±0.02	0.40±0.01
GB3D	0.6-0.8	gt	2.42±0.07	8.64±0.45	0.37±0.00	0.45±0.01	0.41±0.01

*used in incubation experiments. gt-goethite, sh-schwertmannite and qz-quartz.

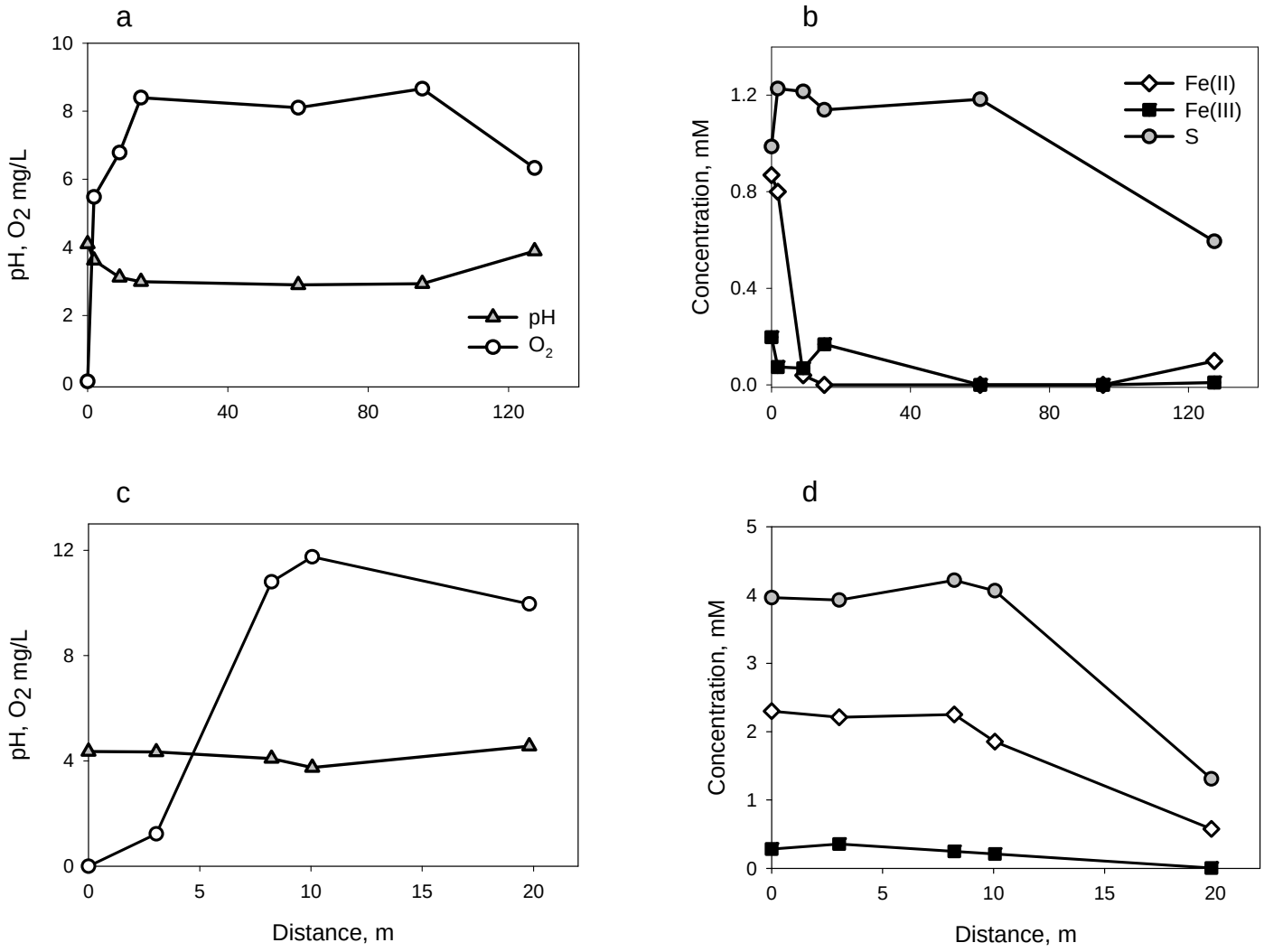
a
pH, O2 mg/L
pH
O2
b
Concentration, mM
Fe(II)
Fe(III)
S
c
pH, O2 mg/L
Distance, m
d
Concentration, mM
Distance, m

Fig. 1.

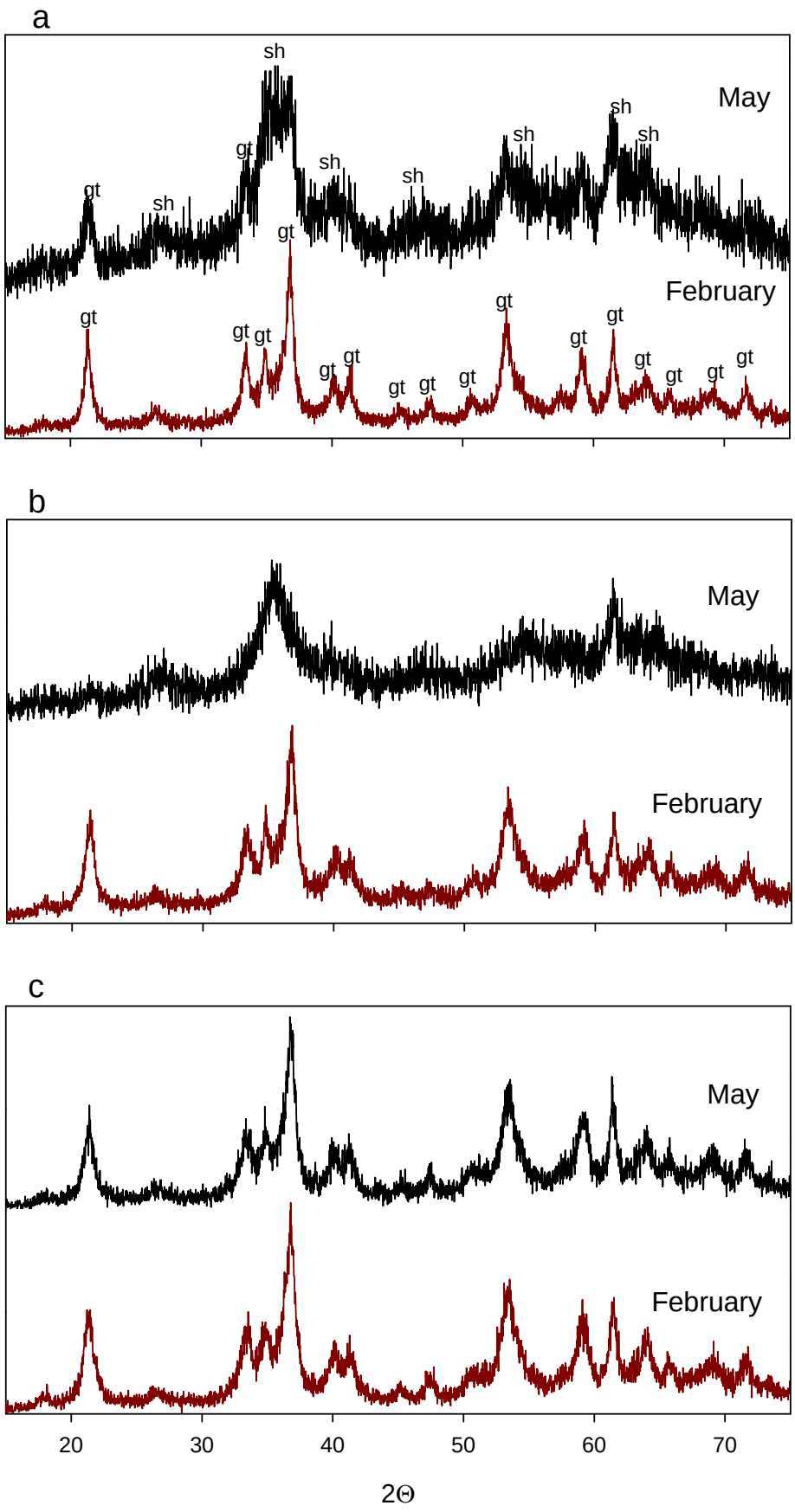
a
May
February
gt
sh
b
May
February
c
May
February
20
30
40
50
60
70
2Θ

Fig. 2.

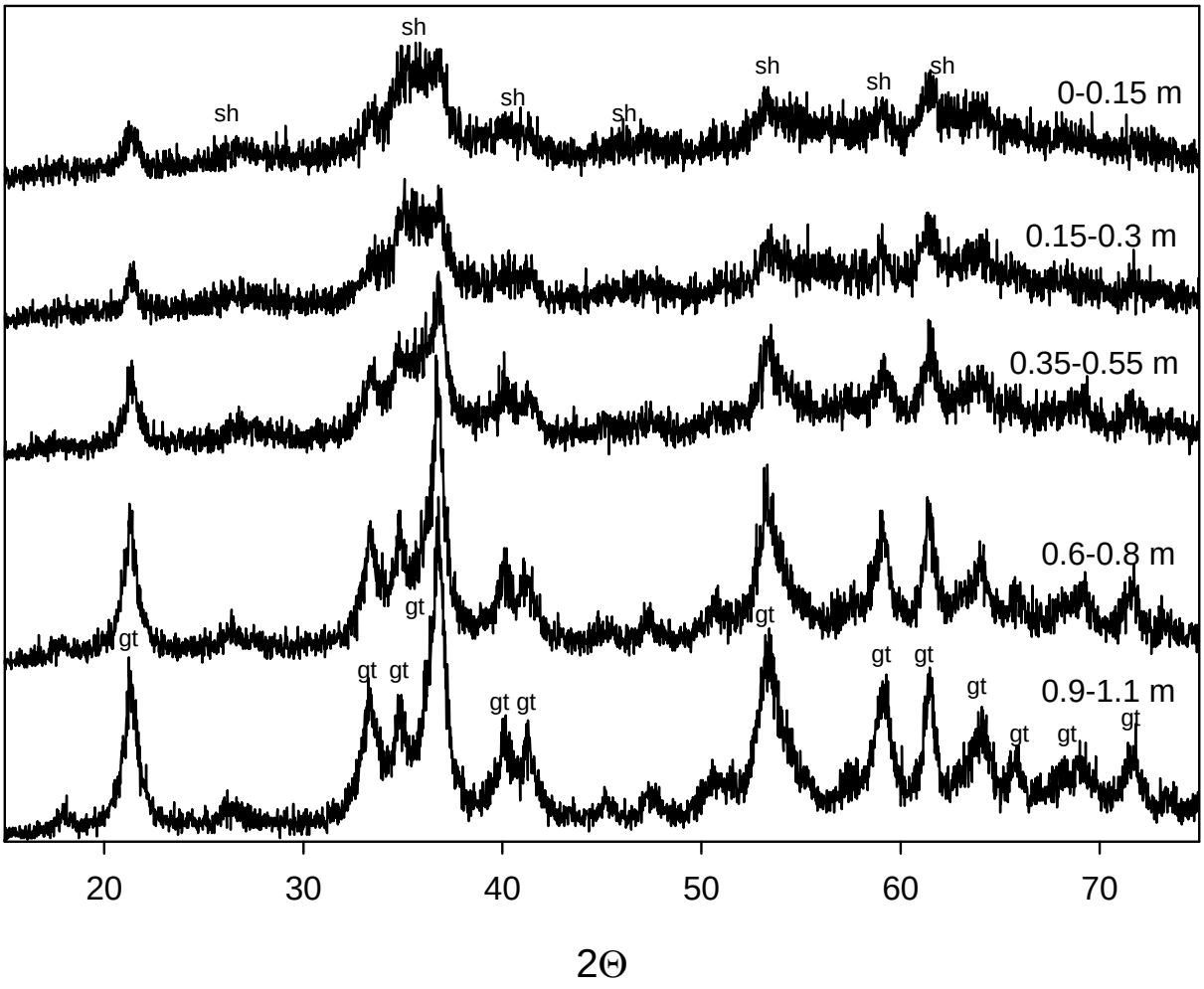
sh
sh
sh
sh
sh
sh
sh
0-0.15 m
0.15-0.3 m
0.35-0.55 m
gt
gt
gt
0.6-0.8 m
gt
gt
gt
gt
gt
gt
gt
gt
gt
0.9-1.1 m
20
30
40
50
60
70
2Θ

Fig. 3.

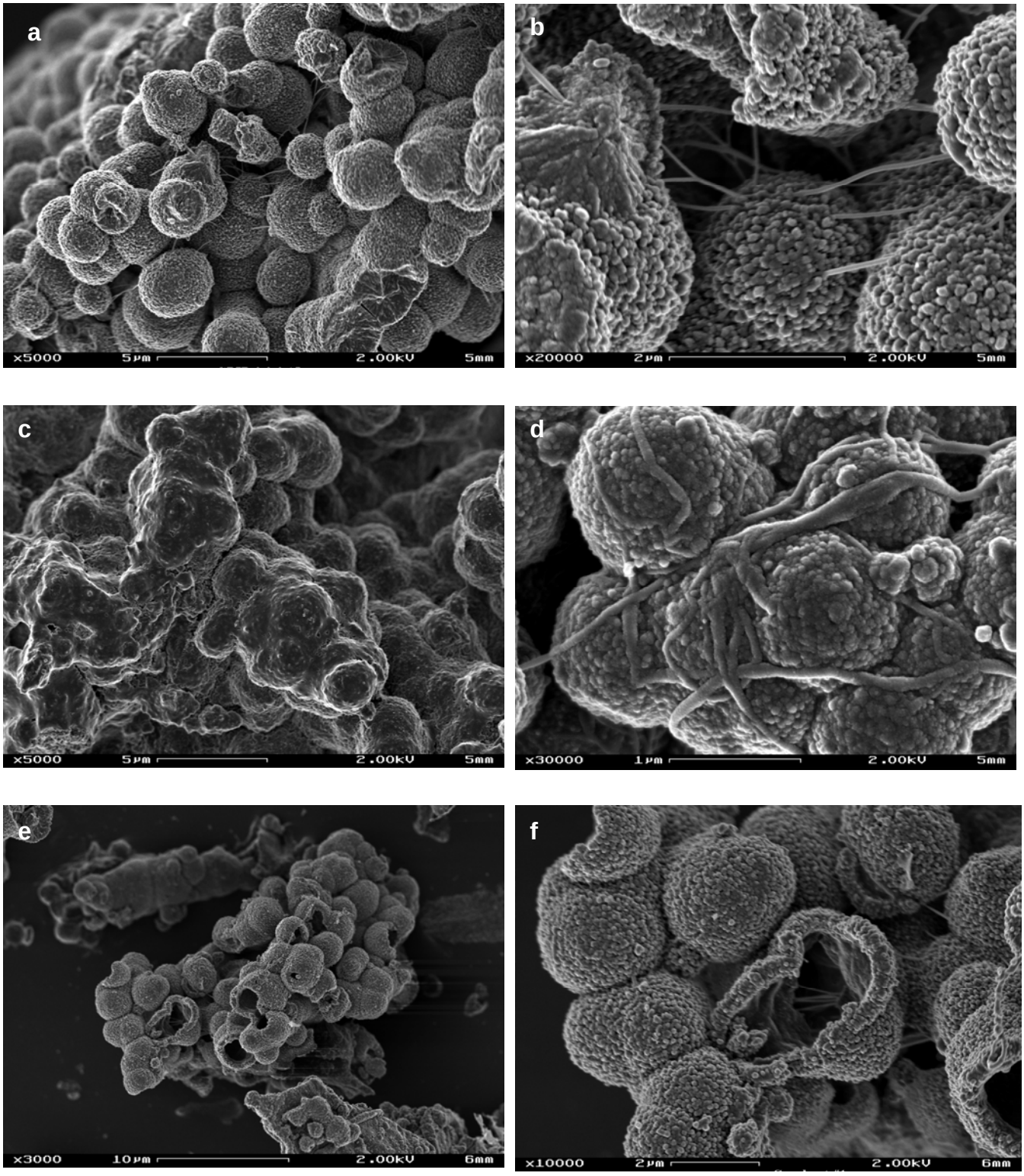
a
x5000 5µm 2.00kV 5mm
b
x20000 2µm 2.00kV 5mm
c
x5000 5µm 2.00kV 5mm
d
x30000 1µm 2.00kV 5mm
e
x3000 10µm 2.00kV 6mm
f
x10000 2µm 2.00kV 6mm

Fig. 4.

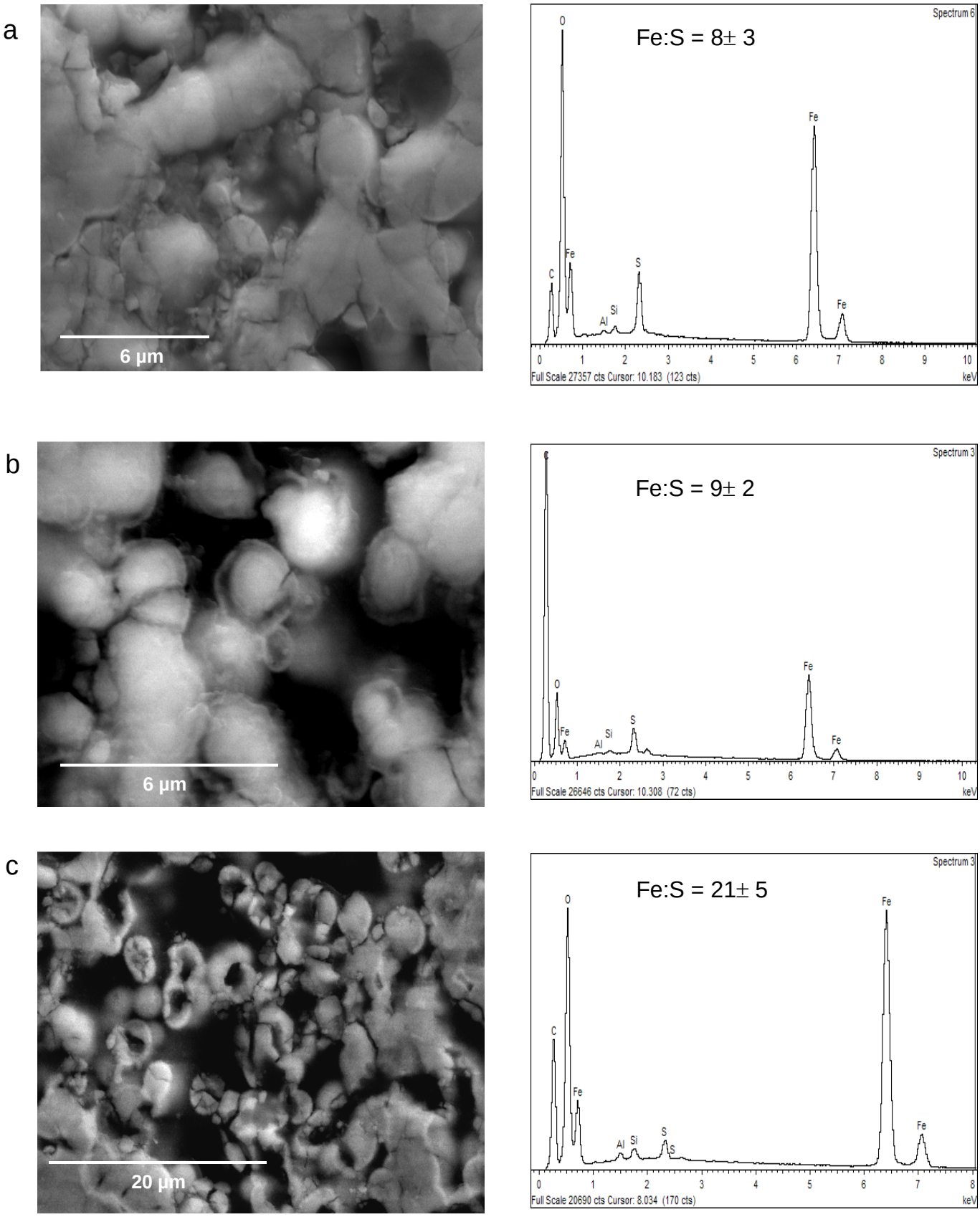
a
6 µm
Spectrum 6
Fe:S = 8± 3
O
Fe
C
Fe
S
Si
Al
Fe
0 1 2 3 4 5 6 7 8 9 10
Full Scale 27357 cts Cursor: 10.183 (123 cts)
keV
b
6 µm
Spectrum 3
Fe:S = 9± 2
Fe
O
Fe
Si
Al
S
Fe
0 1 2 3 4 5 6 7 8 9 10
Full Scale 26646 cts Cursor: 10.308 (72 cts)
keV
c
20 µm
Spectrum 3
Fe:S = 21± 5
O
Fe
C
Fe
Al
Si
S
S
Fe
0 1 2 3 4 5 6 7 8
Full Scale 20690 cts Cursor: 8.034 (170 cts)
keV

Fig. 5.

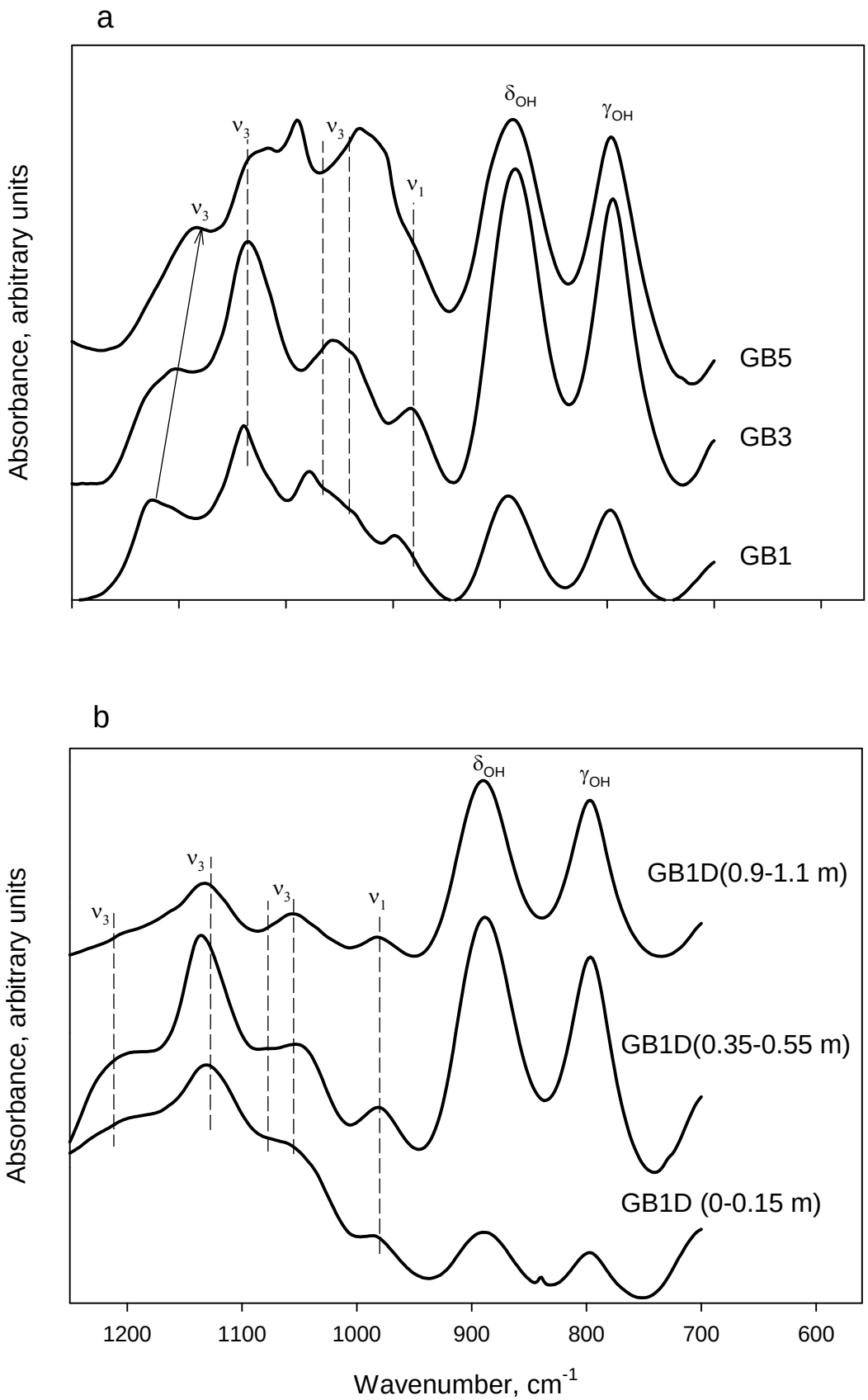
a
Absorbance, arbitrary units
ν_3
ν_3
ν_3
ν_1
δ_{OH}
γ_{OH}
GB5
GB3
GB1
b
Absorbance, arbitrary units
ν_3
ν_3
ν_3
ν_1
δ_{OH}
γ_{OH}
GB1D(0.9-1.1 m)
GB1D(0.35-0.55 m)
GB1D (0-0.15 m)
1200
1100
1000
900
800
700
600
Wavenumber, cm^{-1}

Fig. 6.

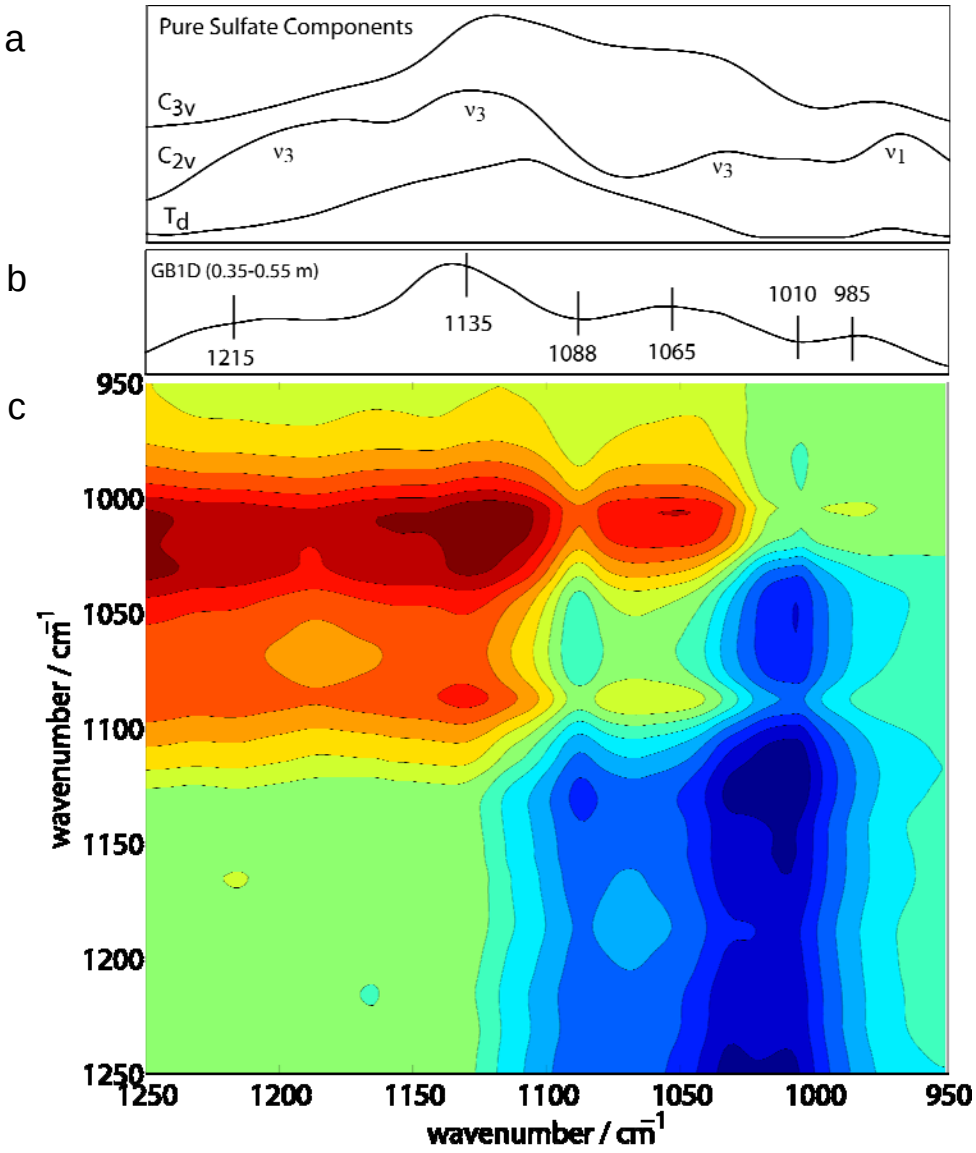
a
Pure Sulfate Components
C3v
C2v
Td
ν3
ν3
ν3
ν1
b
GB1D (0.35-0.55 m)
1215
1135
1088
1065
1010
985
c
wavenumber / cm-1
950
1000
1050
1100
1150
1200
1250
wavenumber / cm-1

Fig. 7.

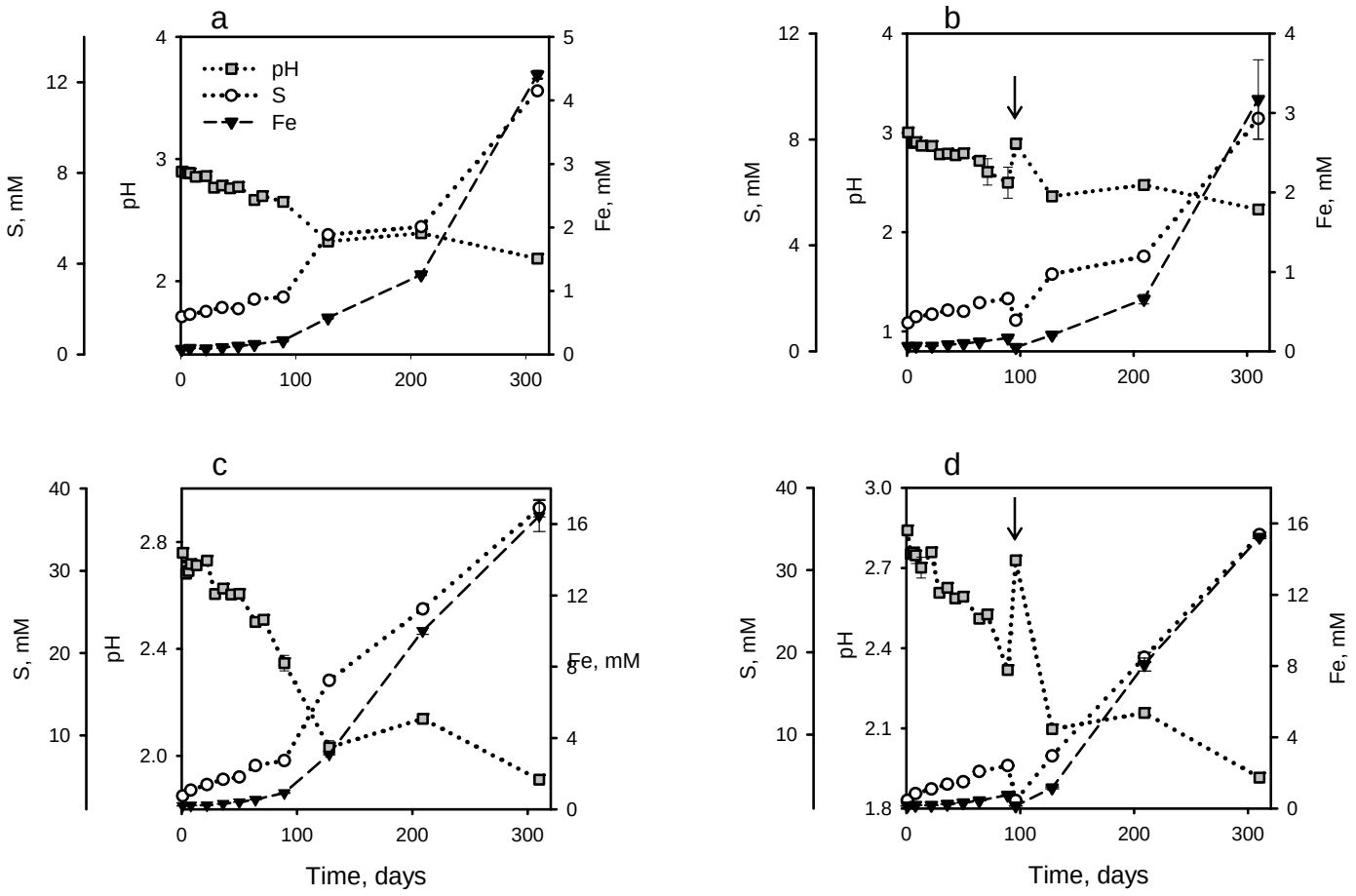

Fig. 8.

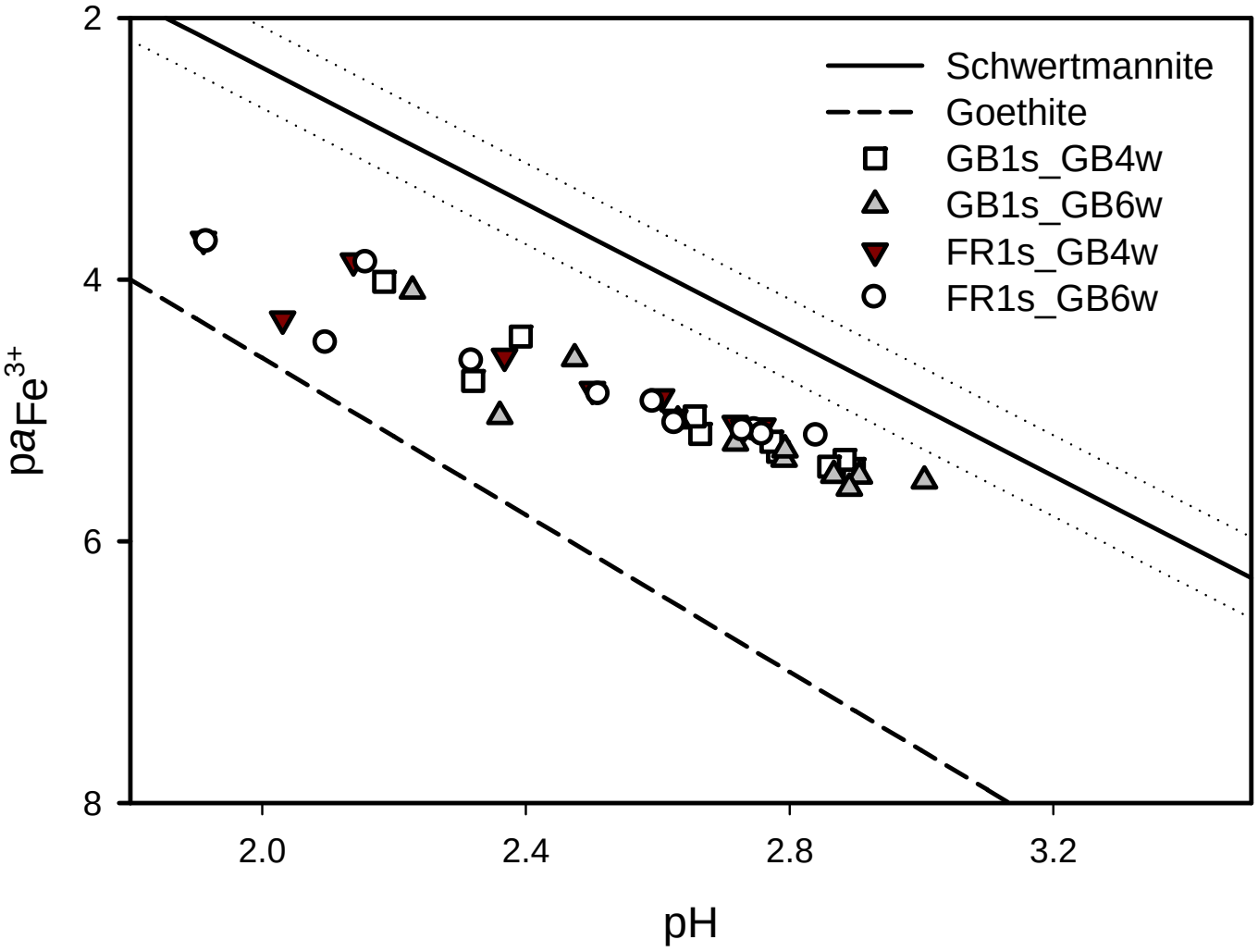
Schwertmannite
Goethite
GB1s_GB4w
GB1s_GB6w
FR1s_GB4w
FR1s_GB6w
2
4
6
8
2.0
2.4
2.8
3.2
pH
pa$_{Fe^{3+}}$

Fig. 9.

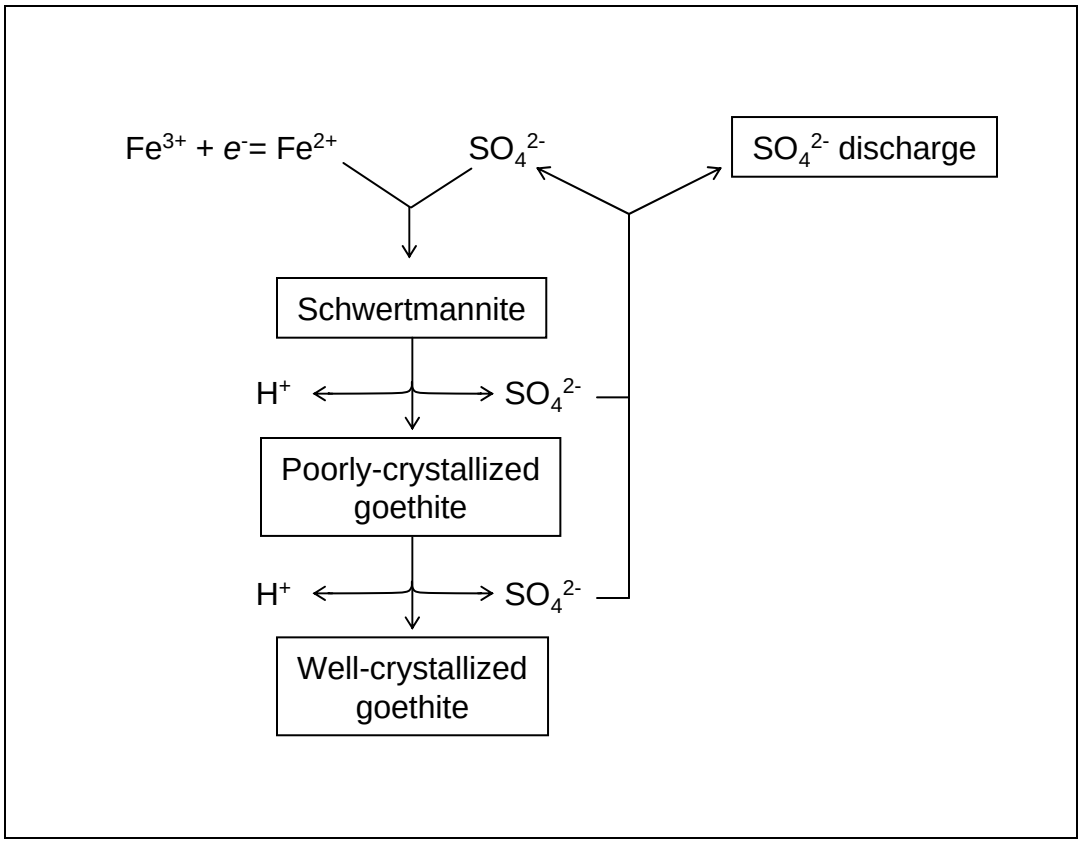
Fe3+ + e-= Fe2+
SO4 2-
SO4 2- discharge
Schwertmannite
H+
SO4 2-
Poorly-crystallized goethite
H+
SO4 2-
Well-crystallized goethite

Fig. 10.